Mechanics of Taylor impact testing of polycarbonate

Sai Sarva, Adam D. Mulliken, Mary C. Boyce *

Department of Mechanical Engineering, Institute for Soldier Nanotechnologies, Massachusetts Institute of Technology,
77 Massachusetts Avenue, Cambridge, MA 02139, USA

Abstract

The deformation of polymers under high-rate loading conditions is a governing factor in their use in impact-resistant applications, such as protective shields, safety glass windows and transparent armor. In this paper, Taylor impact experiments were conducted to examine the mechanical behavior of polycarbonate (PC), under conditions of high strain rate ($\sim 10^5 \, \text{s}^{-1}$) and inhomogeneous deformation. High-speed photography was used to monitor the progression of deformation within the sample. A recently developed three-dimensional large strain rate-dependent elastic–viscoplastic constitutive model which describes the high-rate behavior of glassy polymers was used together with the ABAQUS/Explicit finite-element code to simulate several Taylor impact conditions. The simulation results are compared directly with experimental images for a range in initial rod dimensions and velocities. Final deformed shapes are found to correspond with those obtained experimentally, demonstrating the ability to predict complex inhomogeneous deformation events during very high-rate impact loading scenarios. The dependence of the observed behaviors on the various features of the polymer stress–strain behavior are presented in detail revealing the roles of strain softening and strain hardening in governing the manner in which deformation progresses in a polymer during dynamic inhomogeneous loading events.
© 2006 Elsevier Ltd. All rights reserved.

Keywords: Glassy polymers; Polycarbonate; High-rate testing; Taylor impact; Constitutive model; Plasticity

1. Introduction

The study of the dynamic mechanical properties of materials has garnered an increasing interest over the past few decades after the introduction of the split Hopkinson pressure bar (SHPB), also known as the Kolsky bar (Kolsky, 1949). Since its inception, several modifications have been incorporated into the SHPB to optimize its operation for various loading conditions, materials and strain rates. The strain rates during a SHPB test normally range from about 5×10^2 to $10^4 \, \text{s}^{-1}$ and the highest strain rates that can be nominally achieved are in the range of $(2.5–4.5) \times 10^4 \, \text{s}^{-1}$ (Jia and Ramesh, 2004). However, even these strain rates are nearly an order of magnitude lower than those commonly encountered during some important impact loading events

---

* Corresponding author. Tel.: +1 617 253 2294; fax: +1 617 258 8742.
  E-mail addresses: saisarva@mit.edu (S. Sarva), mcboyce@mit.edu (M.C. Boyce).

such as the striking of a projectile or blast loading. Ultra-high strain rates can be reached during flyer-plate experiments, but these tests require elaborate experimental and specimen preparation techniques.

Sir Taylor devised a simple experiment, subsequently named the Taylor-anvil or Taylor-impact test, to estimate the dynamic yield stress of metals (Taylor, 1948). The test constitutes normally impacting cylindrical projectiles onto a large, rigid, smooth-faced anvil at velocities in the range of 100–200 m s^{-1}, resulting in their non-uniform deformation. Strain rates of 10^5 s^{-1} or higher can be easily attained. Assuming a rigid, perfectly-plastic material model, Taylor determined a relationship between the dynamic yield stress and residual geometry measurements. In conjunction with Taylor's analysis, Whiffin (1948) and Carrington and Gayler (1948), conducted experimental work to study the properties of various steels, duralumin, copper, lead and other metals. Numerous researchers proposed further analyses to improve upon Taylor's original theory (e.g., Hawkyard et al., 1968; Hawkyard, 1969; Wilkins and Guinan, 1973) addressing increasingly detailed aspects of the material behavior (e.g., Jones et al., 1987, 1997, 1998; Gillis et al., 1987; House et al., 1995).

Currently, the Taylor test is primarily used in combination with numerical simulations as a valuable tool in validating constitutive models for various ductile materials due to the large deformation, large gradients of deformation and stress, unique deformation profiles and very high strain rate that can be achieved in this test. For example, Holt et al. (1994) studied the impact deformation of titanium and through computational modeling explained the significance of twinning on dynamic behavior. Such methods are particularly helpful for anisotropic materials, where further insight can be gained by studying the asymmetric deformation of the rod cross-section (e.g., Maudlin et al., 1999, 2003).

A literature search reveals hundreds of papers related to experimental and/or modeling studies on Taylor tests of metallic materials, demonstrating the test's wide spread use in studying high-rate behavior of metals. In contrast, the study of polymers using the Taylor test configuration has been largely unexplored. A handful of experimental results have been reported. Briscoe and Hutchings (1976) tested high density poly(ethylene) (HDPE) and observed that the calculation of yield stress using Taylor's theoretical analysis resulted in inaccuracies due to the exclusion of elastic strains. Hutchings (1979) proposed an alternate one-dimensional elastic–plastic wave propagation analysis to calculate the yield stress in polymers and compared it with Taylor's analysis using experimental data on polycarbonate. Millet et al. (2006) studied the behavior and failure initiation of poly(ether ether ketone) (PEEK) at velocities in the range of 150–400 m s^{-1} using high-speed photography. Rae et al. (2004) studied the high temperature behavior of poly(tetrafluoroethylene) (PTFE). Turgutlu et al. (1996) varied the nose-geometries of high and low density poly(ethylene) (HDPE and LDPE) samples to numerous axially symmetric concave and convex designs to further the understanding of mushrooming of polymeric samples. The study of polymers under Taylor test loading conditions in association with finite-element simulations has not yet been conducted.

Significant advances have been made in determining the temperature and rate-dependent constitutive behavior of glassy polymers and the underlying deformation micro-mechanisms (e.g., Boyce et al., 1994; Boyce et al., 1988; Arruda and Boyce, 1993). Mulliken and Boyce (2006) have recently further enhanced these previous constitutive models to incorporate mechanisms that are activated during high loading rates. In this paper, Taylor impact tests are conducted to probe the behavior of PC under inhomogeneous loading conditions at rates greater than those achieved with SHPB testing. The deformation events incurred during Taylor impact tests are numerically simulated and understood, utilizing finite element analysis together with a physically-based constitutive model of the high-rate behavior of the polymeric solids.

2. Review of stress–strain behavior of polycarbonate

Polycarbonate was chosen for the present study since it is extensively used due to its excellent combination of stiffness, strength, toughness, ductility, impact resistance and transparency. It is well known that the stress–strain behavior of glassy polymers exhibits a strong strain rate and temperature dependence. It has also been observed for various polymers that there exists a transitional threshold in rate and temperature beyond which the strain-rate sensitivity significantly increases. The Ree and Eyring theory (1955) accounts for multiple activated processes and provides the most widely accepted theory of rate-dependent yield, to help capture the yield behavior of polymers across this threshold. These thermally activated processes have been related to transitions observed in the viscoelastic spectra. Using data over a wide range in temperatures, but at quasi-static

strain rates (10^{-4}–10^{-1} s^{-1}), Bauwens (1972) related this transition in rate sensitivity to the secondary β transition. Mulliken and Boyce (2004, 2006) have recently identified and quantitatively characterized this same β transition to be relevant at high strain rates.

Mulliken and Boyce (2006) have conducted dynamic mechanical analysis (DMA) to characterize the viscoelastic behavior of PC with focus on rate-dependent shifts of material transitions. PC was tested over a range of temperatures (−140 °C to 180 °C) at 1 Hz, 10 Hz and 100 Hz. These frequencies corresponded to average strain rates of 1.9×10^{-3} to 3.2×10^{-1} s^{-1} for the particular specimen dimensions. Fig. 1 shows the storage modulus and loss tangent curves for a test at 1 Hz. As is well known, the storage modulus drops drastically at the glass (α) transition. The loss modulus curve exhibits maxima at transitions and helps to accurately identify the locations of the α and β transitions. For PC, the β transition is around −90 °C and it is sufficiently decoupled from the α transition, which is around 145 °C. With decreasing temperature, the storage modulus increases from about 2 GPa to 3 GPa as the β transition is surpassed. These transitions undergo a temperature shift with increasing strain rate. Fig. 1 also shows the shift in α and β transitions for tests at two different frequencies. This shift was observed to be different for the two transitions. The α transition was observed to shift ∼5 °C per decade of strain rate and the β transition shifts almost 15 °C per decade of strain rate over the range of accessible rates in the DMA.

Based upon the DMA test data, Mulliken and Boyce (2004, 2006) predict the elastic behavior over a wide range of strain rates and temperatures. An expression for the elastic modulus was developed by first decomposing the storage modulus into its respective α and β components. Fig. 2 shows the elastic moduli predicted over a range of strain rates by properly shifting the α and β regions of the curve. Fig. 2 predicts that for PC, at room temperature, a change in the rate sensitivity of the mechanical behavior will occur at a strain rate of ∼10^2 s^{-1}.
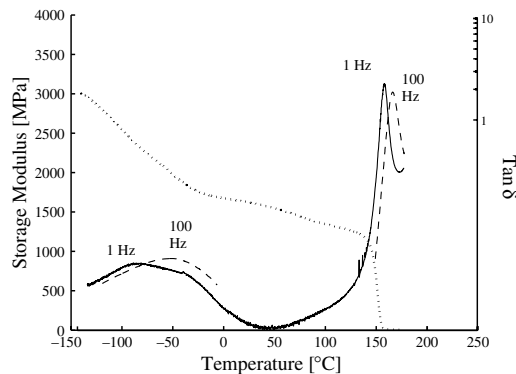

Fig. 1. Representative storage (dotted line) and loss tangent for PC for a test performed at 1 Hz; shift in loss tangent for PC at 100 Hz in the α and β transition regions is also shown (Mulliken and Boyce, 2006).
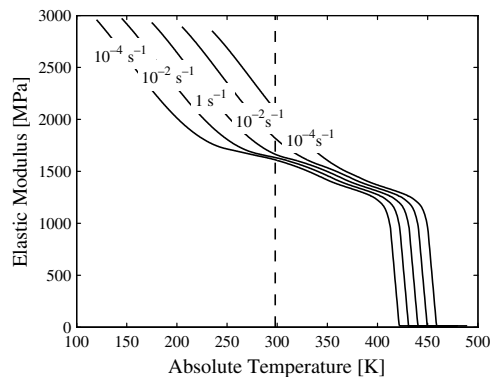

Fig. 2. Predictions of the elastic moduli curves made by the decompose/shift/reconstruct method (Mulliken and Boyce, 2006).

Large deformation uni-axial compression tests were conducted on PC from low (10^{-3} s^{-1}) to high strain rates (10^3 s^{-1}) to determine the rate dependence of the yield and post-yield behavior (Mulliken and Boyce, 2006). Fig. 3(A) shows the stress–strain curves for PC at different strain rates. Yield is well defined and followed by strain softening and subsequent strain hardening. Rate sensitivity is manifested in the form of increasing yield and flow stress, with increasing strain rate. Fig. 3(B) shows the yield stress plotted against strain rate. Two distinct regions of strain rate sensitivity are observed. This indicates the occurrence of a significant material transition in the intermediate region resulting in this increased rate sensitivity. Upon extrapolation, it was estimated that the location of this transition lay around 1.5×10^2 s^{-1} at room temperature. This estimation is in good agreement with the transition prediction made using the DMA data. This insight concerning the strain-rate sensitivity of the viscoelastic transitions formed the foundation of the development of a new constitutive model.

Constitutive models to describe three-dimensional, temperature and rate-dependent, finite-strain deformation of thermoplastic materials have been developed, for example, by Boyce et al. (1988); Arruda and Boyce (1993) and Boyce et al. (1994), and experimentally validated at low to moderate strain rates and temperatures, for a variety of homogeneous and inhomogeneous loading conditions where the strain rates were less than 5 s^{-1}. Recently, a rate-dependent three-dimensional constitutive model, developed by Mulliken and Boyce (2006), extends the predictive capabilities to high rates and low temperatures. Fig. 4 shows the 1-D rheological
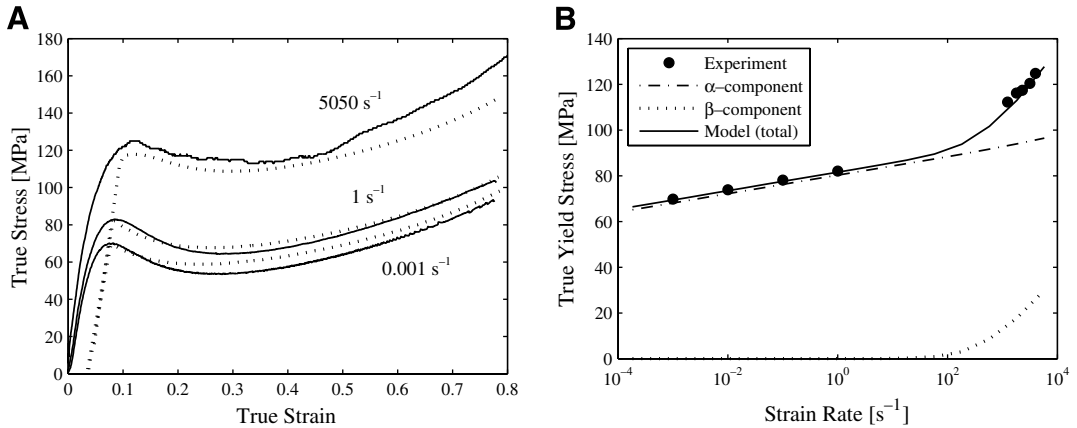

Fig. 3. (A) Experimental and model results of the uni-axial compressive stress–strain behavior over a range in strain rates; (B) yield stress (data and model predictions) as a function of strain rate (Mulliken and Boyce, 2006).
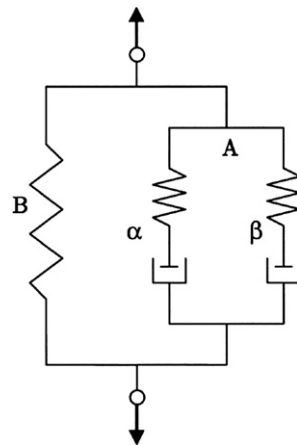

Fig. 4. 1-D interpretation of the constitutive model (Mulliken and Boyce, 2006).

interpretation of the new model. Segment B is a non-linear Langevin spring, which represents the molecular network resistance to stretching and alignment. Segment A has two sub-segments (α and β) in parallel, each with an elastic spring and visco-plastic dashpot in series. Segment A represents the intermolecular resistance to chain-segment rotation. The two sub-segments (α and β) indicate two distinct thermally-activated processes, associated with different molecular-level motions. For PC, the α process relates to the rotation of the polymer main chain and the β process to the local rotations of main-chain phenyl group. At high temperatures and low strain rates, the contributions due to the β component are minimal and intermolecular resistance is primarily due to the α process. However, at higher rates/lower temperatures, the β process must be activated adding to the intermolecular resistance. The complete three-dimensional, finite-strain kinematical details and material description can be found in Mulliken and Boyce (2006).

Fig. 3 demonstrates the accuracy of the model in describing the high-rate behavior of PC. Fig. 3(A) shows the predicted stress–strain curves plotted against the experimentally obtained curves at three different strain rates. Fig. 3(B) displays the model predictions[1] plotted against the experimentally observed yield stress values over seven orders of magnitude of strain rate. The yield stress values from α and β components are also plotted. The significance of the identification of the contribution made by the β process and its successful implementation into the constitutive model is evident. High-rate deformation is often accompanied by adiabatic heating, which affects the constitutive behavior. Presently, these effects have been neglected since the amount of thermal softening in PC has been found to be small (Mulliken and Boyce, 2006); efforts are underway to incorporate the effects of adiabatic heating into the constitutive model (Mulliken, 2006) following the model of Arruda et al. (1995).

3. Investigation protocol

3.1. Experiments: Taylor impact tests

The Taylor tests were conducted at the MIT Institute for Soldier Nanotechnologies' high-rate laboratory. Flat-ended cylindrical specimens were impacted normally onto a smooth-faced rigid tile to induce deformation. The cylinders shortened in length in a non-uniform manner, manifesting a mushroom head at the impact end. The tests were performed on PC cylinders with a diameter of 12.7 mm. Their length ranged from 25.4 mm to 76.2 mm. The velocity was varied from ~180–280 m s^{-1} to vary the stress and strain-rate conditions. These velocities were below the critical velocity above which failure was induced in the samples.

A 12.7 mm diameter bore single stage gas gun was used to perform the Taylor impact tests. The barrel was 2.13 m long and the breech was capable of pressures up to 690 bar. A double diaphragm assembly was burst to propel the polymeric cylinder at the requisite speed through the barrel. The diaphragm material was chosen to be aluminum or Mylar®, depending on the breech pressure. Nitrogen was used as the pressurizing gas. The impact velocity typically reached up to 300 m s^{-1} when the breech pressure was of the order of 70 bar. A hardened stainless steel tile, 100 mm × 100 mm wide and 12.7 mm thick, was mounted on a steel frame and clamped on the top and bottom edges and acted as the rigid surface. The impact face of the stainless steel tile was ground to a smooth finish. It was also lubricated to help reduce friction during impact. The initial velocity of the specimen was measured with laser ribbon inter-valometers. Two parallel laser ribbons were placed 152.4 mm apart across the line of flight and their intensity was monitored with photodiodes. The specimen, during its flight, interrupted the ribbons and registered its presence successively on the photodiodes. The time delay between the successive triggering of the photodiodes was used to calculate the velocity. The specimens impacted onto the stainless steel block, deformed, rebounded and were later recovered and examined. The steel tile showed no signs of deformation or bending, during or after the test. The distance between the muzzle

---

[1] The material parameters used in Mulliken and Boyce (2006) constitutive model are as follows: the storage modulus as a function of strain rate and temperature, Poisson ratio $(\nu_\alpha) = (\nu_\beta) = 0.38$; pre-exponential factors $(\gamma^p_{0,\alpha}) = 2.94 \times 10^{16}$ s^{-1}, $(\gamma^p_{0,\beta}) = 3.39 \times 10^5$ s^{-1}; activation energies $(\Delta G_\alpha) = 3.744 \times 10^{-19}$ J, $(\Delta G_\beta) = 3.769 \times 10^{-20}$ J; softening slope $(h_\alpha) = 250$ MPa; ratio of initial to steady state intrinsic resistance $(s_{0,\alpha}/s_{ss},\alpha) = 0.58$; pressure coefficients $(\alpha_{p,\alpha}) = 0.168$, $(\alpha_{p,\beta}) = 0.245$; limiting chain extensibility $(\sqrt{N}) = 1.516\sqrt{m}$; rubbery modulus $(nk\theta) = 14.2 \times 10^6$ MPa; density $(\rho) = 1300$ kg m^{-3}; specific heat $(C_p) = 1200$ J(kg K)$^{-1}$; strain rate threshold $(\dot{\varepsilon}_{th}) = 1 \times 10^{-4}$ s^{-1}.

and the steel tile was ∼2 m. The gas gun was operated remotely for safety purposes using actuator controlling instrumentation. Also, the gas gun was an enclosed type, where the specimen impact area was located within a protective steel chamber and isolated from the surroundings.

A Cordin rotating mirror high-speed CCD camera with a Nikon 70–300 mm lens, capable of acquiring images at a frame rate of 2 million frames per second, was used to photographically record the event. The camera was triggered by the initial velocity sensor and a built-in trigger delay was used to synchronize it with the impact event. The camera in turn triggered a high performance strobe for better illumination. The camera was programmed to record a sequence of 32 separate images at prescribed time intervals. Images were acquired from a point of view normal to the flight path of the specimen cylinder. High-speed photography is especially essential for studies of polymeric materials, where large strain recoveries can occur.

3.2. Material

PC was chosen for the study since it is used in a wide range of applications which require impact resistance together with transparency. A machine grade PC was procured from GE polymer shapes. The grade of PC used for this study, was slightly different than the one used in the Mulliken and Boyce (2006) study (Lexan™ PC 9034), due to the availability of just one grade in the rod form from GE Plastics. The material was obtained in 12.7 mm diameter, 2.4 m length extruded rod form and cylinders were further machined from the rods. The diameter was reduced to 12.67 mm to help smooth movement in the gas gun barrel. 25.4 mm and 76.2 mm length cylindrical samples were made and the flat ends were polished. Due to the extrusion process, the molecular chains were expected to exhibit some alignment. However, compressive Hopkinson bar tests ($\sim 4 \times 10^3\,\mathrm{s}^{-1}$) showed the material to be fairly isotropic and have a behavior nearly identical to Lexan™ PC 9034.

3.3. Finite element modeling

The constitutive model, outlined in Section 2 and described in Mulliken and Boyce (2006), was numerically implemented into a commercial finite element code, ABAQUS/Explicit through an user-defined material sub-routine. Numerical simulations were conducted to study the stress and deformation conditions in polymeric cylinders under impact. Simulations were performed for the same impact velocities and cylinder lengths as those used for the experiments. The cylinder was modeled as axi-symmetric and four-node quadrilateral reduced-integration elements were used. The contact between the cylinder and the steel surface was assumed to be frictionless. A simulation was also performed in which the cylinder was modeled in 3-D, with eight-node
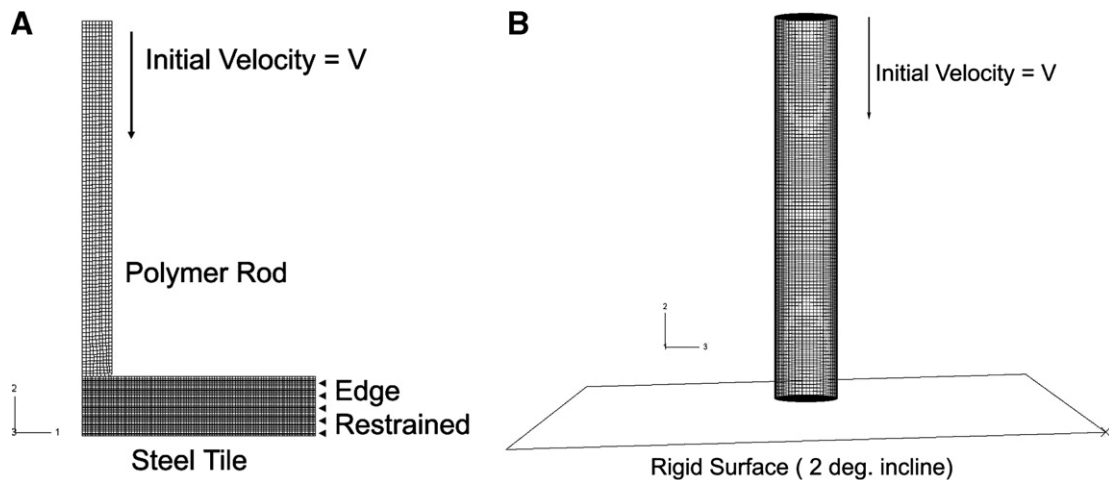

Fig. 5. (A) Sample geometry and boundary conditions used for a 2-D axi-symmetric simulation of Taylor test; (B) sample geometry for a 3-D simulation.

solid elements to help account for a slight yaw of the cylinder during one of the experiments. The initial velocity imparted to the cylinder was used as the boundary condition. The termination time for the simulations was chosen such that the sample had sufficiently recoiled after impact. Fig. 5(A) shows the geometry of the 76.2 mm long PC cylinder and the steel tile that was used for a 2-D axi-symmetric simulation of impact. Fig. 5(B) shows the geometry for a 3-D simulation. For the 3-D simulation, the impact plate was modeled as a rigid surface instead of a steel tile to make the computation less time intensive. The mesh density was varied from coarse to fine to verify that the chosen mesh provided accurate solutions. A combined viscous-stiffness form of hourglass control (weight factor = 0.5) was used for both the 2-D and 3-D simulations. No significant variation in results was observed when the viscous-stiffness weight factor was varied from 0 (no damping) to 1 (pure damping).

4. Results and discussion

Experiments were conducted on 12.7 mm diameter cylinders at impact velocities varying from ~180–280 m s^{-1}. Two sample lengths, representing short and long rods were chosen: 25.4 mm and 76.2 mm (L/D ratios of 2:1 and 6:1, respectively). The velocity was increased to increase the extent of deformation. Results are presented for a few representative cases in the form of photographs of the progression of the deformation event, followed immediately by the finite element simulations for the same loading conditions.

4.1. Taylor impact test on a 76.2 mm rod at 187 m s^{-1}

4.1.1. Normal impact

Fig. 6 shows a montage of high-speed images for a test conducted on a 76.2 mm cylinder at 187 m s^{-1}. The time intervals for the individual frames are as shown. The rod was illuminated from the rear, since silhouettes provide a more discerning view of the profiles during the event. The impact is normal and the deformation is fairly symmetric. The cylinder is seen to impact the steel tile in frame 2, sending a deformation front down the cylinder. The deformation results in the formation of a mushroom head, which enlarges as the event progresses, along with radial barreling above the mushroom head. The cylinder continues to deform in a non-uniform and plastic manner for about 100 µs. After some additional duration of contact, the cylinder begins to rebound. The cylinder displays some elastic recovery during this duration of contact and its rebound. After impact, the residual rod shape shows a plastic radial expansion over approximately one-half the length with a slight lip at the impact end.

An axi-symmetric simulation of the test (Fig. 6) was performed using the mesh geometry and boundary conditions described in Fig. 5(A). The montage in Fig. 7 shows the rod geometry prior to impact and a sequence of predicted shapes at time intervals corresponding to the high-speed photographs. The computed profiles match well with the photographic images. Detailed features of the chronology of loading and elastic recoil events are reproduced. The deformed head of the rod, which shows a slight lip close to the impact end in the high-speed pictures, as well as the radial barreling are also captured in the simulation.
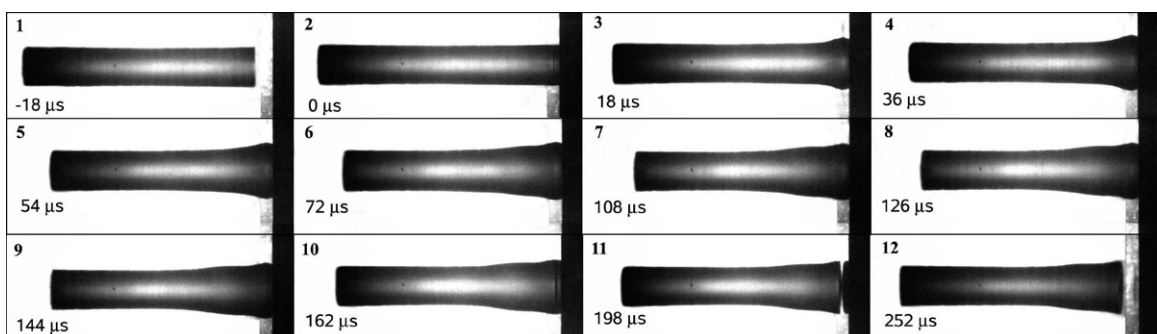

Fig. 6. High-speed silhouette photographs recorded at various stages during a Taylor test on a 76.2 mm rod at 187 m s^{-1}.
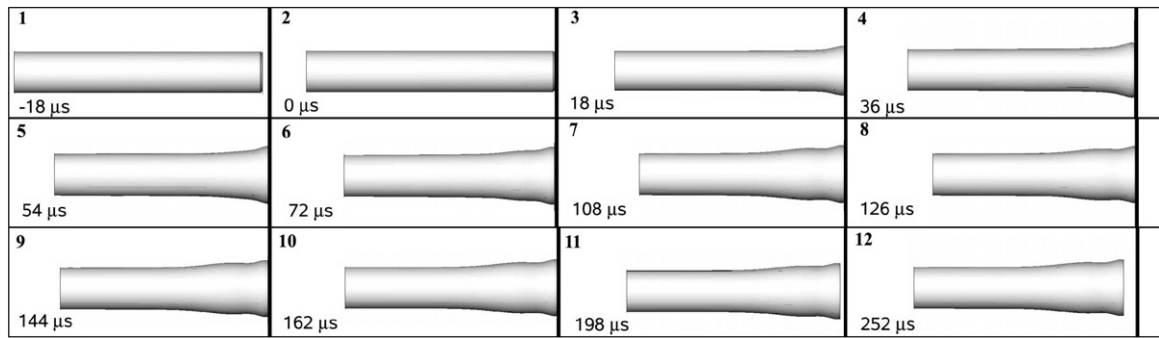
Fig. 7. Deformation profile predictions made using axi-symmetric simulation of the 76.2 mm rod test at 187 m s^{-1}.

The simulation was used to gain an understanding of stress and deformation conditions that exist during the event. Fig. 8 shows axial stress contours at various stages of impact. Extremely high compressive stress is induced immediately upon impact at the head, where the stress magnitude exceeds 450 MPa during the initial 3 μs. Within 6 μs, the peak stress magnitude drops to less than 300 MPa. At 12 μs, concentrated regions of high axial tensile stress (>90 MPa) are formed. These observations indicate the highly transient nature of the stress induced during the initial few microseconds after impact. Such a transient regime has been identified for various impact events by many researchers in other materials; see, for example, Jones et al. (1992). By 30 μs, the compressive wave front is fairly stabilized and proceeds towards the rear end of the cylinder, inducing deformation during its travel. At 51 μs, this compressive wave front reaches the rear end of the cylinder. The deforming profile shows that the initial compressive front is followed by a slower moving plastic deformation front, also traveling towards the rear of the sample. As this plastic front proceeds, the front-end of the cylinder forms a mushroom head. In the meantime, the initial elastic compressive front, reflects back from the rear end as a tensile front, and interacts with the compressive waves that are still emanating from the impact surface. The plastic deformation subsequently subsides as seen by the profiles at 102 μs and 150 μs. By 200 μs, the cylinder has begun to rebound. As is observed, the reflection and interaction of the stress waves continues during rebound. The extent of rebound at specific intervals after impact is also observed to match well with the high-speed photographs.

Fig. 9 shows the evolution of pressure in the cylinder at the same time intervals as in Fig. 8. The cylinder is subjected to intense positive and negative pressures. During the initial highly transient regime, pressures ranging from 340 MPa to −100 MPa are reached.[2] By the end of the deformation event, the pressure drops to less than a few MPa.

Fig. 10 shows the evolution of plastic strain rate in the cylinder which indicates the regions of material that are actively plastically deforming at that instant. During the initial 3 μs, plastic strain rates as high as $6.5 \times 10^4 \, \text{s}^{-1}$ are attained. Peak strain rate drops to ∼$4 \times 10^4 \, \text{s}^{-1}$ within the next 3 μs, and successively diminishes to a few thousand per second by 51 μs. These contours reveal how the rod plastically deforms to achieve the final shape of a radial bulge with a distinguishing lip at the impact end; in particular, this lip is seen to be due to angular shear bands which form at the early stages of impact. Negligible amounts of plastic deformation are observed in the cylinder during its rebound as seen in the profile at 300 μs. These observations clearly indicate the extreme nature of stress and deformation gradients induced in a sample cylinder during a Taylor test.

The cylinder was recovered and the residual geometry was studied and photographed. The residual rod confirmed the high-speed photographic observations that deformation was ductile with no signs of failure. Fig. 11(A) shows a comparison of the experimentally observed residual rod geometry with that predicted

---

[2] We note that under moderate strain rate loading events, isotropic PC cavitates and fails in a brittle manner when experiencing hydrostatic stresses of ∼80 MPa (Nimmer and Woods, 1992; Socrate and Boyce, 2000; Johnson, 2001). Cavitation and failure are not observed in this experiment, perhaps due to the small time duration of negative pressure or due to the correspondingly increased modulus at this strain rate decreasing the volumetric strain associated with this negative pressure.
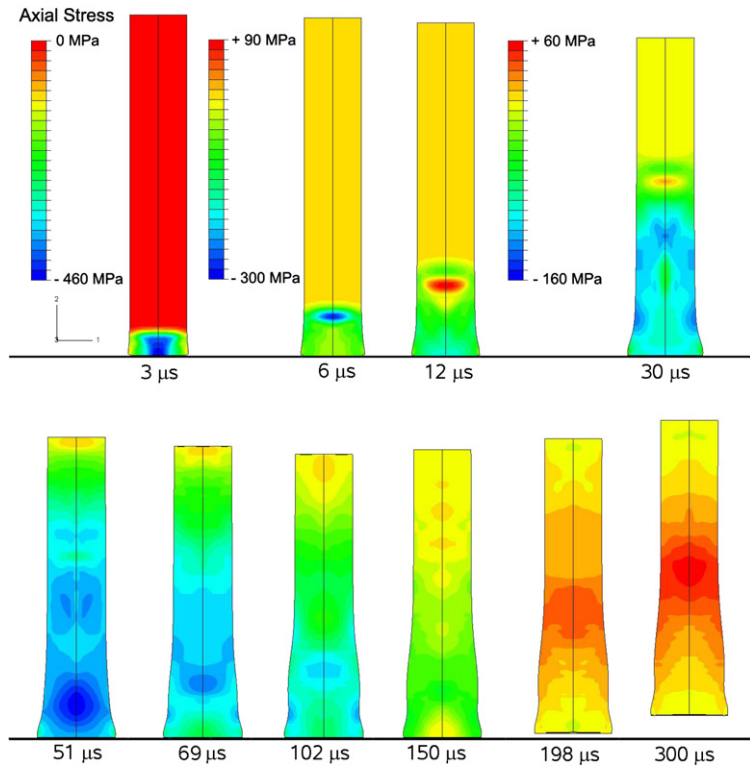
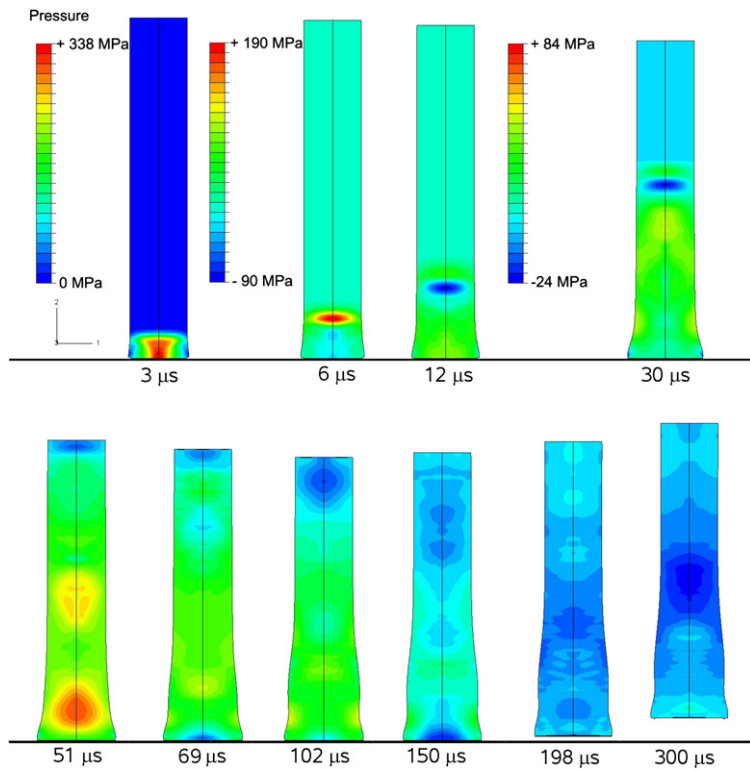Fig. 8. Contours of axial stress at various stages for a test on a 76.2 mm cylinder at 187 m s^{-1}.

Fig. 9. Contours of pressure at various stages for a test on a 76.2 mm cylinder at 187 m s^{-1}.
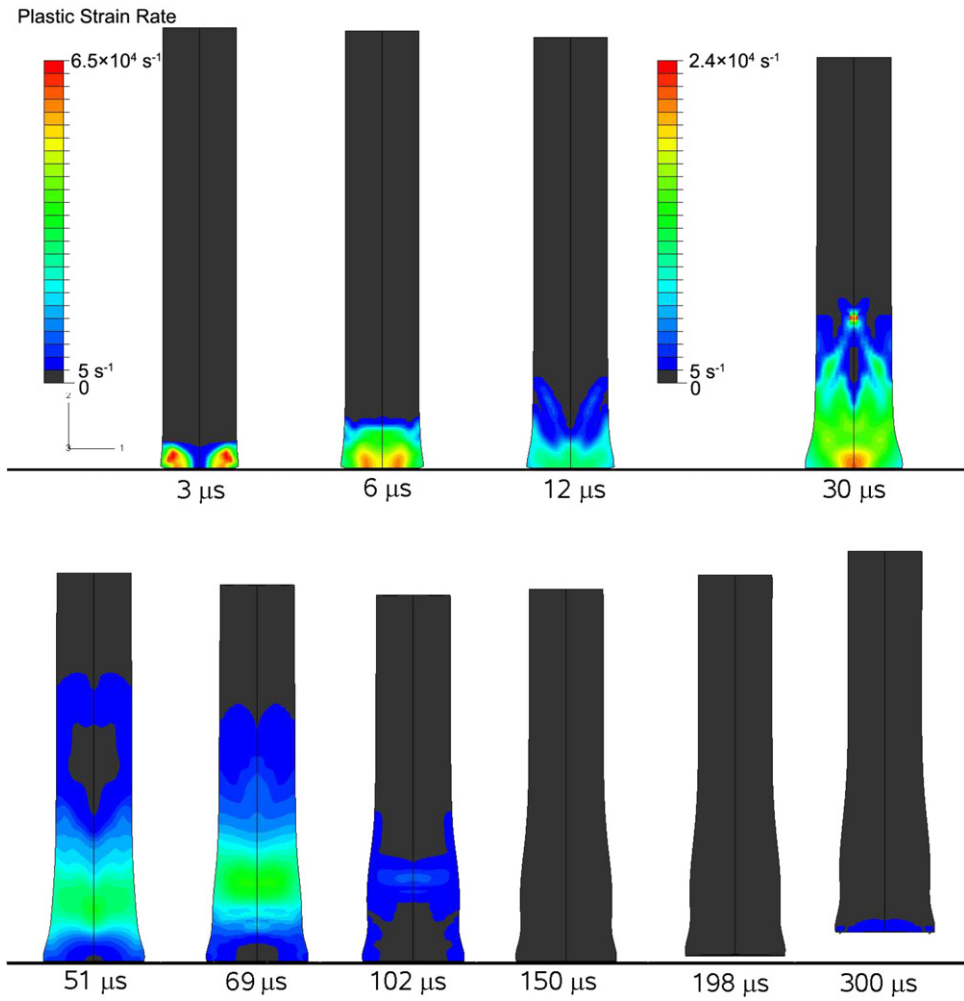
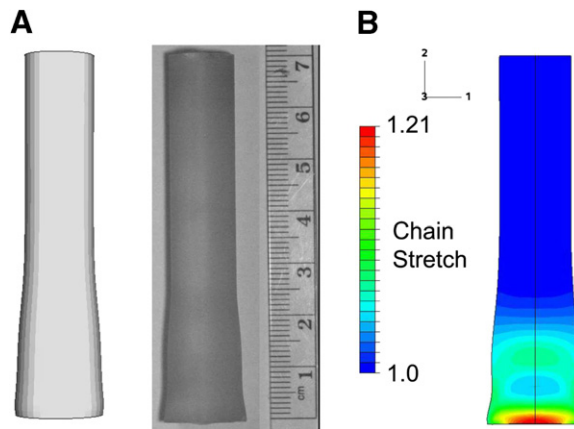Fig. 10. Contours of plastic strain rate ($\dot{\gamma}_\alpha$) at various stages for a test on a 76.2 mm cylinder at 187 m s^{-1}.

Fig. 11. (A) Comparison of a 360° axi-symmetric sweep with recovered cylinder for a test on a 76.2 mm cylinder at 187 m s^{-1}; (B) contours of chain stretch.
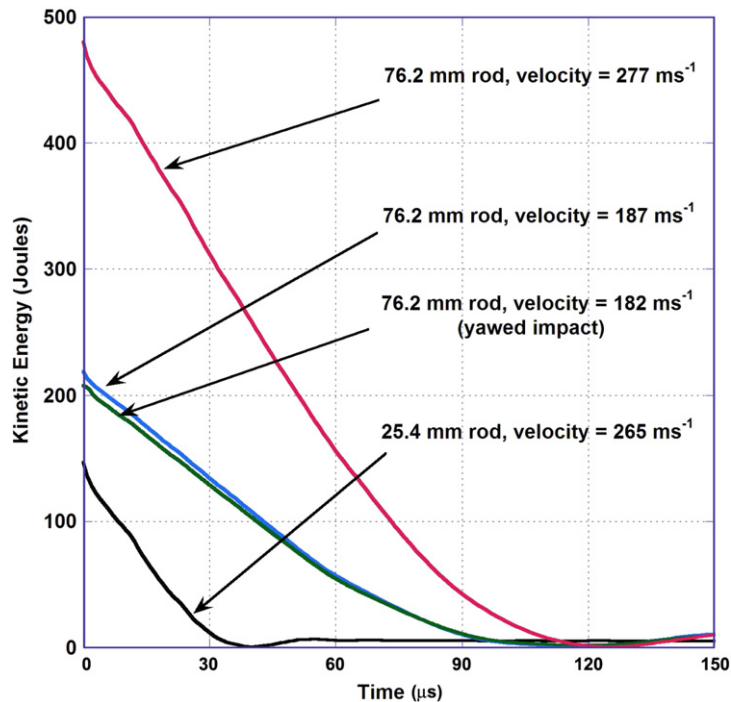
Fig. 12. Simulated kinetic energy profiles for Taylor tests under various impact conditions.

by the finite element simulation. As can be seen, the finite element model accurately predicts the overall geometry, including the final shortened length, the ratio of deformed and undeformed lengths, and the shape of the mushroom head. Fig. 11(B), displaying the chain stretch[3] (λ_{chain}) in the residual rod, gives a further comparison of the deformed and undeformed regions of the cylinder. The stretch contours indicate that large deformation gradients exist along the axis of impact and also across the cross-section of the cylinder.

The simulation of decay in the kinetic energy (KE) of the rod is plotted in Fig. 12. Consistent with the above observations, it is observed that by 150 μs, the initial KE has been consumed and rebound has begun. Fig. 12 also includes the KE profiles for rods impacted at various test conditions that are discussed in the later sections.

4.1.2. The effect of yaw on the Taylor test

Tests were also conducted to study the effect of yaw on the deformation of the cylinder. Fig. 13 shows a montage of high-speed images for a test in which a 76.2 mm cylinder impacts the rigid plate at 182 m s^{-1} with a slight yaw. The frames are ~50 μs apart. The yaw is determined to be 2° from the photographs. The cylinder impacts the steel tile in frame 2. In frames 2 and 3, some lubricant in seen jetting away from the impact interface. The deformation is observed to be slightly asymmetric due to the yaw. The asymmetry results in the lip that is formed near the impact end to be more pronounced on one side. The yaw also induces some bending in the rod as seen in frames 5–8. During its rebound and elastic recovery, the cylinder displays some recovery of bending as seen by the straightening of the cylinder in frames 7 and 8.

The test shown in Fig. 13 was numerically simulated to examine the ability of the computational model to capture the effect of yaw. A 3-D simulation was performed using the geometry described in Fig. 5(B). The geometry incorporates the 2° yaw. The montage in Fig. 14 shows the rod geometry prior to impact and a sequence of predicted shapes at successive intervals of 50 μs. As is observed, the asymmetry in deformation and features such as bending, elastic recovery and their chronology are accurately reproduced.

---

[3] Stretch on a chain in an eight-chain network $\lambda_{chain} = \sqrt{\mathrm{trace}\,(\overline{\mathbf{B}}_{\mathbf{B}})/3}$, where $\overline{\mathbf{B}}_{\mathbf{B}} = (\det \mathbf{F})^{-2/3} \mathbf{F}\mathbf{F}^{\mathrm{T}}$ and $\mathbf{F}$ is the deformation gradient.
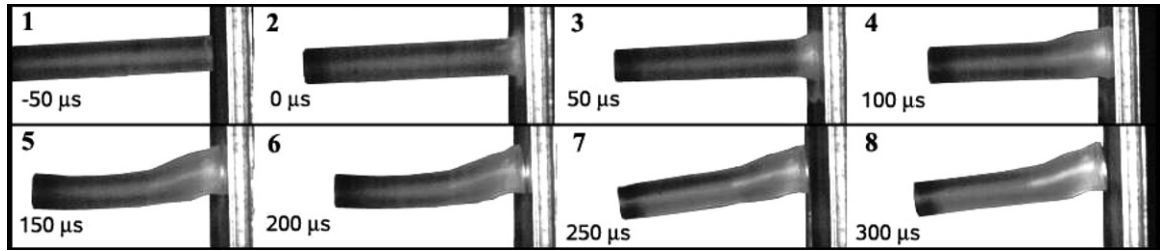
Fig. 13. High-speed photographs recorded at various stages during a Taylor test on a 76.2 mm rod at 182 m s^{-1} with a 2° yaw (frame interval ∼ 50 μs).
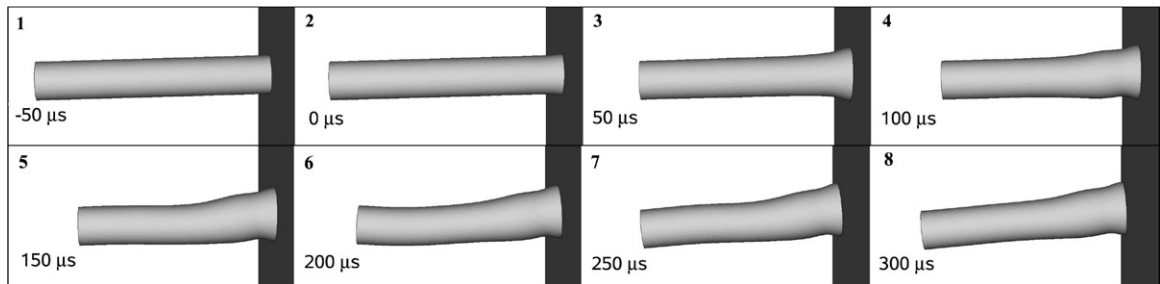

Fig. 14. 3-D simulation of the Taylor test on a 76.2 mm rod at 182 m s^{-1} with a 2° yaw (interval ∼ 50 μs).
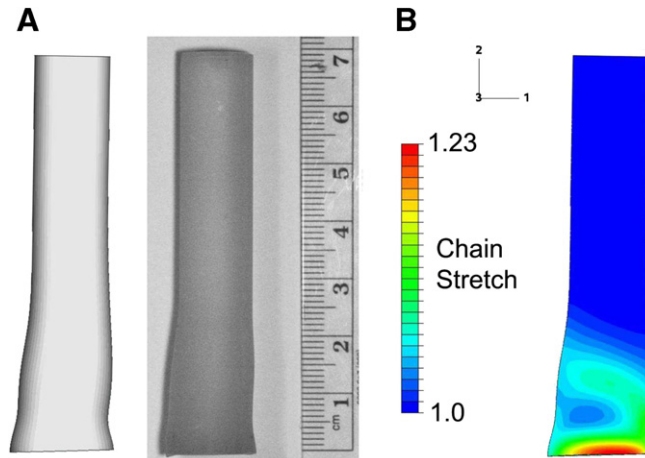

Fig. 15. (A) Comparison of simulation with residual shape of the 76.2 mm rod impacted at 182 m s^{-1} with a 2° yaw; (B) contours of chain stretch.

Fig. 15 shows that the simulation accurately captures the effect of yaw on the residual rod shape. Contours of chain stretch are also plotted to indicate the asymmetry in deformation.

4.2. Taylor impact test on a 76.2 mm rod at 277 m s^{-1}

To study the effect of impact velocity, tests were conducted on 76.2 mm rods at velocities that were ∼100 m s^{-1} higher than the previous test. Fig. 16 shows a sequence of high-speed images for such a test at 277 m s^{-1}. Frame 2 was captured a few microseconds after impact. Frame 8 shows the rod at ∼100 μs after
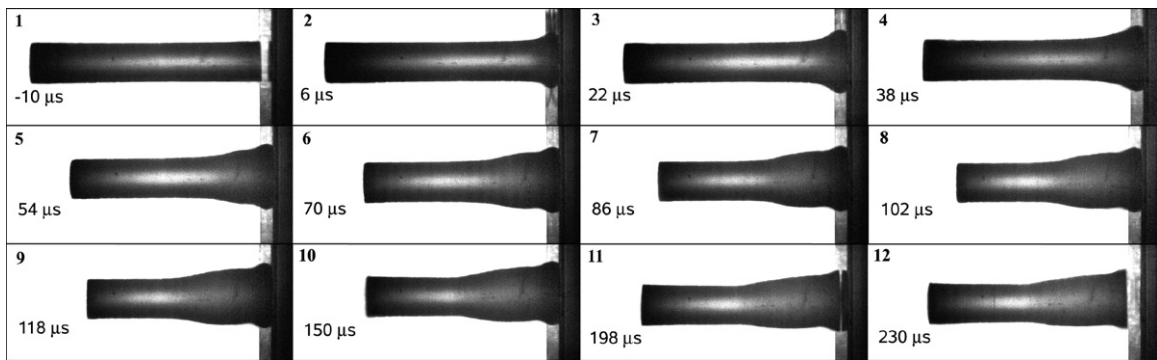
Fig. 16. High-speed silhouette photographs recorded at various stages during a Taylor test on a 76.2 mm rod at 277 m s^{-1}.

impact and frame 10 at ~150 μs after impact. Similar to the test with an impact velocity of 187 m s^{-1}, the rod continues to heavily deform during the initial ~100 μs. The rod undergoes greater amounts of deformation as displayed by an increased overall shortening and wider mushrooming of the head. By ~200 μs, the rod shows signs of rebound. These pictures indicate that compared to the test at 187 m s^{-1}, the event duration has not changed significantly. The additional lip that is formed in the mushroom head is more pronounced at this higher velocity.

The higher velocity test was also numerically simulated as 2-D axi-symmetric to evaluate the stress and deformation conditions. The evolution of compressive stress is plotted in Fig. 17; the time intervals for this figure are chosen to be the same as those plotted for the test at 187 m s^{-1}. As expected, higher magnitudes of stress are induced. During the initial transient regime, the axial stress ranges from 700 MPa (compressive) to 125 MPa (tensile). These values are nearly 50% higher than those for the test at 187 m s^{-1}. Pressure contours (not shown) reveal pressures in the range of 500 MPa to −125 MPa during the initial 12 μs. These values are again nearly 50% higher than those for the test for 187 m s^{-1}.

The increased impact velocity results in a greater mushrooming of the cylinder. The simulation captures the more pronounced lip along the profile, close to the impact end. Similar lips have been commonly observed for Taylor tests performed on metals at high velocities (see Wilkins and Guinan, 1973). Profiles at 102 μs and 150 μs indicate that the plastic deformation is negligible beyond 100 μs. An interesting feature of the test at 277 m s^{-1} is the concave nature of the end of the mushroom head, observed in profiles at 198 μs and 300 μs. Such a concave head has also been observed in polymer tests by Briscoe and Hutchings (1976) and Millet et al. (2006). Contours of plastic strain rate (see Fig. 18) display that strain rates in excess of 10^5 s^{-1} are reached during the initial stages. The contours show the shear banding and evolution in plastic straining that lead to the distinctive lip together with the prominent radial barreling.

The cylinder was again recovered after the test and characterized. Fig. 19(A) shows that the model prediction of the residual shape matches the recovered cylinder. In this higher velocity test, the severity of the additional lip on the mushroom head is also accurately predicted. Fig. 19(B) displays that, as expected, a larger portion of the cylinder has undergone deformation and larger magnitudes and gradients of deformation have been induced in comparison to the test at 187 m s^{-1}.

4.3. Taylor impact test on a 25.4 mm rod at 265 m s^{-1}

Experiments were also conducted on 25.4 mm length rods to study the effect of rod length on the mechanics of Taylor impact tests. Fig. 20 shows a sequence of high-speed silhouette photographs for a test at 265 m s^{-1}. At this velocity, the rod plastically deformed and failure was not induced. The images capture the entire event of impact and rebound. As is observed, the cylinder impacts the rigid plate normally with no visible yaw. Impact occurs in frame 2. By frame 8, approximately 80 μs after impact, rebound of the cylinder is observed. In comparison to the test on a 76.2 mm rod at a similar velocity, the event duration has substantially shortened. Also, the shorter rod length results in a remarkable difference in the profile of the mushroom head.
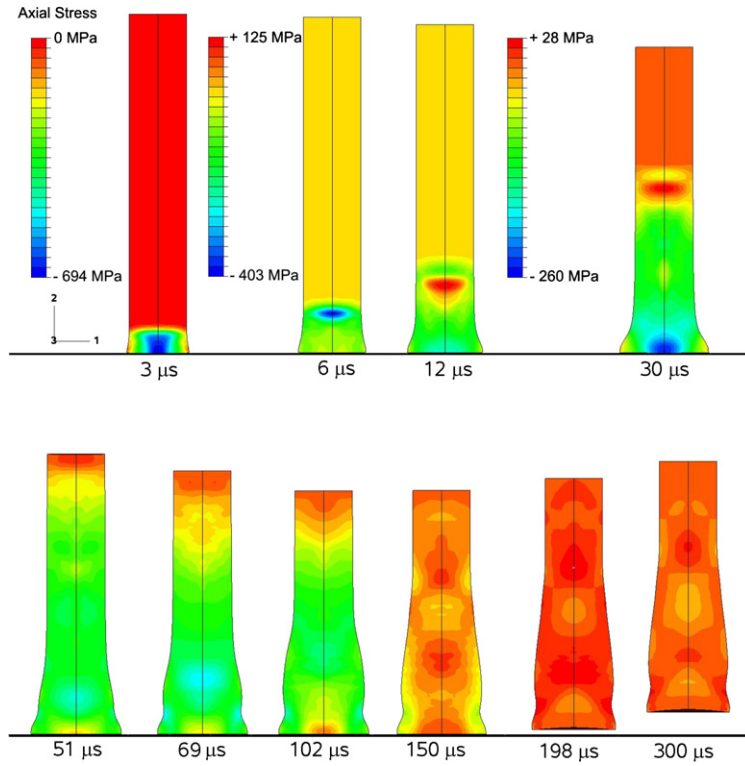
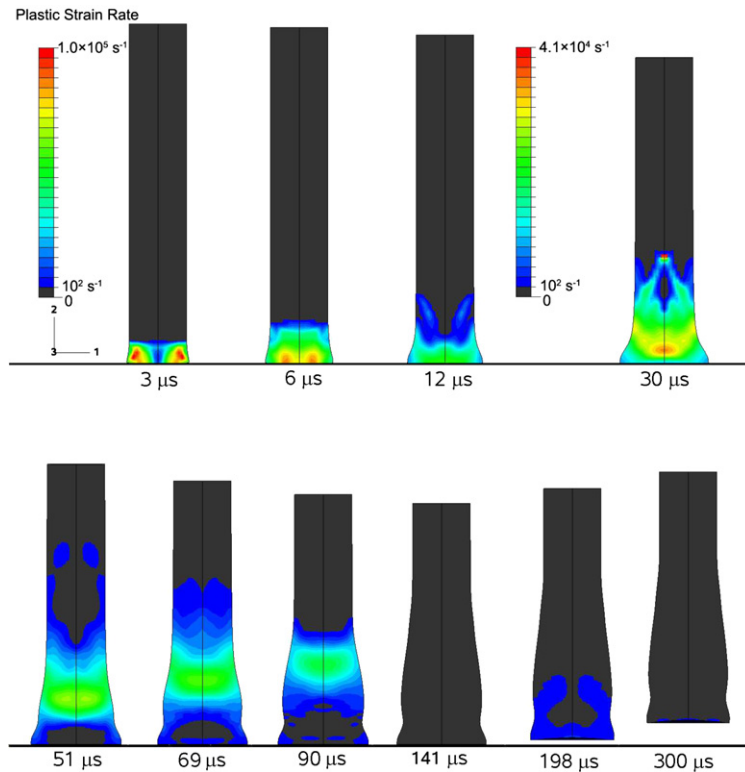Fig. 17. Contours of axial stress at various stages for a test on a 76.2 mm cylinder at 277 m s^{-1}.

Fig. 18. Contours of plastic strain rate $(\dot{\gamma}_\alpha)$ at various stages for a test on a 76.2 mm cylinder at 277 m s^{-1}.
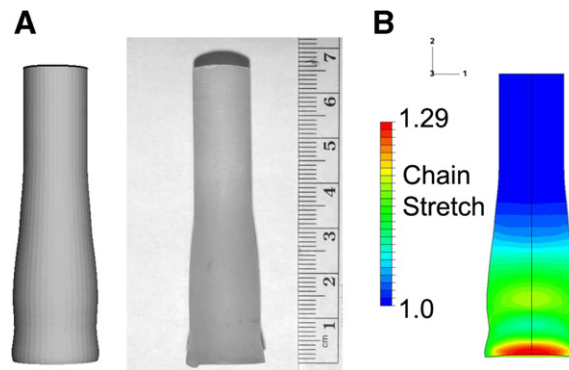
Fig. 19. (A) Comparison of 360° axi-symmetric sweep with recovered cylinder for a test on a 76.2 mm cylinder at 277 m s^{-1}; (B) contours of chain stretch.
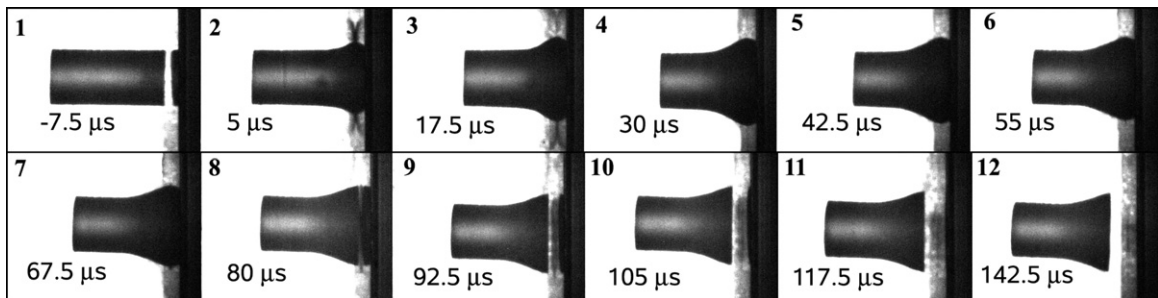

Fig. 20. High-speed silhouette photographs recorded at various stages during a Taylor test on a 25.4 mm cylinder at 265 m s^{-1}.

Similar to the 76.2 mm rod, the impact end shows considerable concavity after rebound but no radial barreling is observed.

The successive photographic rod profiles are again compared with numerical simulations. Figs. 21 and 22 show contours of axial stress and plastic strain rate, respectively. The initial stages show compressive stresses as high as 660 MPa, followed by tensile stresses of nearly 120 MPa. Plastic strain rates of nearly 1.65×10^5 s^{-1} are attained at 1.5 µs after impact, reducing to less than 10^5 s^{-1} at 3 µs. The shear banding which leads to the mushroom head formation is again seen. The simulation captures the shortened event and rod profiles at various time intervals. Rebound is seen to initiate at $\sim$72 µs, similar to photographic observations. The simulated profiles also display the mushroom head to undergo substantial recovery in the radial directions leading to a more pronounced concavity.

Fig. 23(A) shows the comparison of 2-D axi-symmetric sweep of the 25.4 mm rod at 150 µs after impact with a post-mortem photograph of the cylinder. The sweep and the experimental results compare accurately for these test conditions too. Fig. 23(B) shows the contours of chain stretch in the deformed rod. The deformation is largest in a region immediately below the impact surface.

5. The effect of constitutive behavior on the residual rod profile

The constitutive behavior of the polymer governs the deformation characteristics and the resulting residual profile of the Taylor rods. The material parameters in the model (Mulliken and Boyce, 2006) were varied and finite element simulations were performed to isolate the effects of various features of the stress–strain behavior on the resulting rod shapes. This understanding can help guide in utilizing the Taylor test for a qualitative study of polymers with unknown high-rate properties. It can also help guide inverse methodology studies wherein material parameters for models are deduced from residual rod shapes.
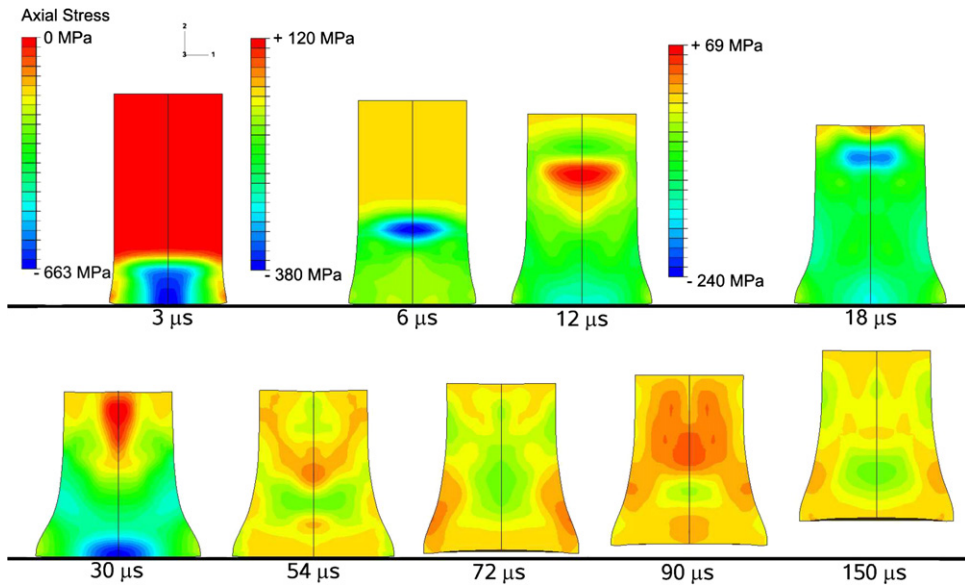
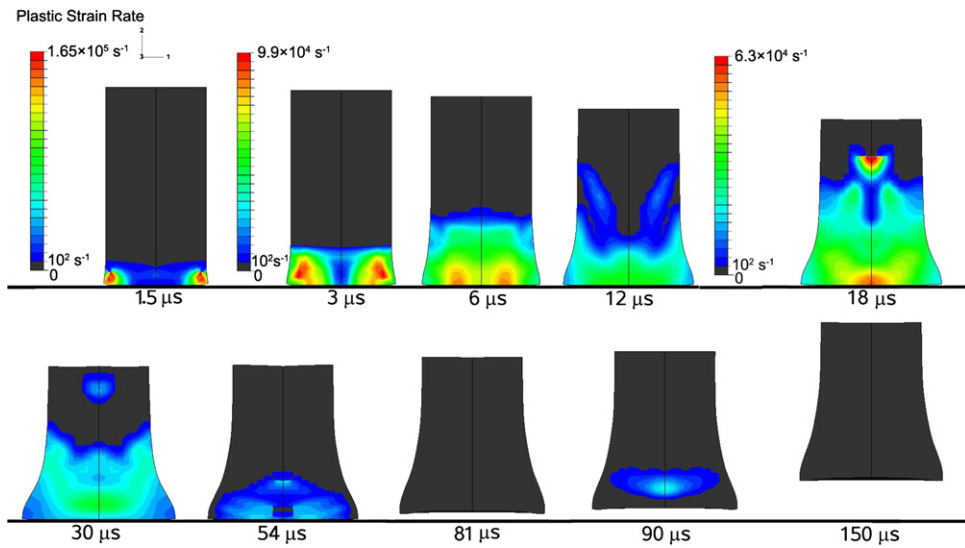Fig. 21. Contours of axial stress at various stages for a test on 25.4 mm cylinder at 265 m s^{-1}.

Fig. 22. Contours of plastic strain rate ($\dot{\gamma}_\alpha$) at various stages for a test on 25.4 mm cylinder at 265 m s^{-1}.
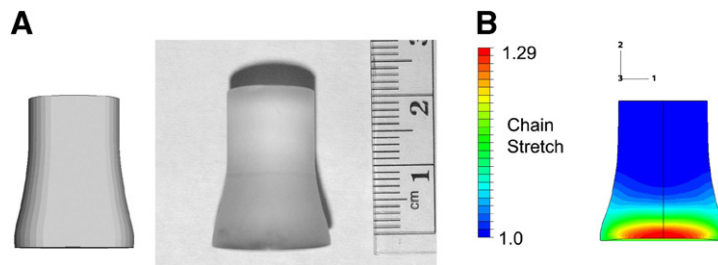

Fig. 23. (A) Comparison of 360° axi-symmetric sweep with the recovered cylinder for a test on 25.4 mm cylinder at 265 m s^{-1}; (B) contours of chain stretch.
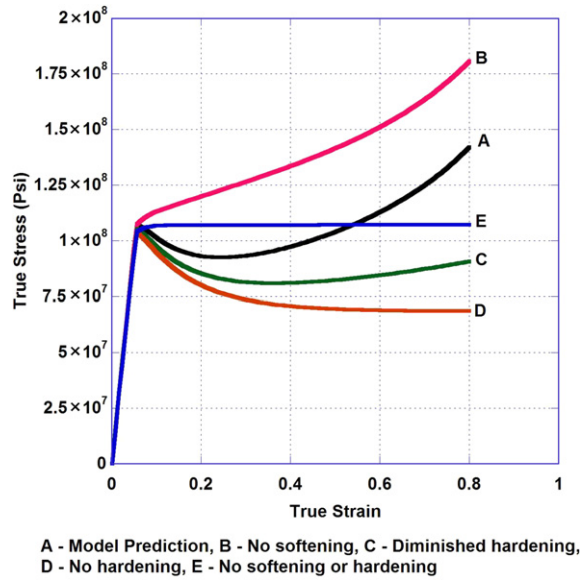
Fig. 24. Comparison of five different cases of stress–strain behavior under uni-axial compression at a strain rate of $10^3 \, \text{s}^{-1}$.

Five different constitutive behaviors were chosen for comparison. Fig. 24 shows the stress–strain curves under uni-axial compression for the five cases at a strain rate of $10^3 \, \text{s}^{-1}$. Curve A shows the actual model prediction, which exhibits features of yield, post-yield softening and strain hardening. In curve B, the softening has been suppressed, resulting in an increased flow stress. In stress–strain curve C, the post-yield softening is maintained but the hardening is reduced by lowering the value of initial strain hardening modulus (C_R) and increasing the value of limiting chain extensibility (N). In stress–strain curve D, the hardening is completely suppressed by further varying the above parameters, resulting in a further drop in the flow stress at high strains. And in curve E, both the softening and hardening have been suppressed resulting in plastic flow at a rate-dependent stress level.
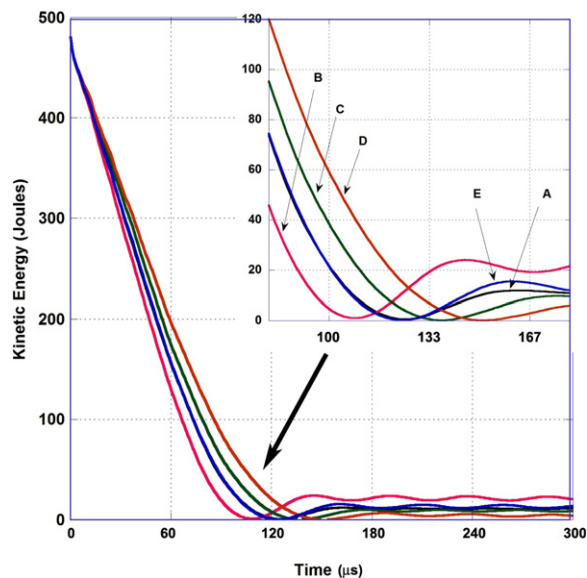

Fig. 25. Effect of variation of stress–strain behavior on the simulated kinetic energy profiles for a 76.2 mm rod impacting at $277 \, \text{m s}^{-1}$.

Fig. 25 shows the simulated time-resolved kinetic energies for a 76.2 mm Taylor rod, impacting at 277 m s^{-1}, described by the above five constitutive behaviors. For case B, the initial KE is arrested in the shortest duration of time indicating shorter duration of deformation due to reduced softening. Also, the KE of rebound is the largest for this case. The time duration for arrest of the initial KE increases successively as the hardening is reduced, which can be attributed to increased deformation needed to absorb the energy of impact. Post-rebound, the residual KE also lowers as the hardening is reduced, giving an additional indication of the greater level of plastic deformation as opposed to elastic deformation occurring in the material during impact. The KE profile for rod with constitutive behavior described by curve E is the closest to the actual model prediction (curve A), since the overall post-yield stress levels for these two cases are the closest.

Fig. 26 shows the residual rod profiles and extent of rebound from impact surface at 300 μs for the five different cases for impact of a 76.2 mm length rod at 277 m s^{-1}. Contours of stretch are plotted to help visualize the extent of deformation. Fig. 26(B) shows that elimination of softening results in reduced concavity of impact face, reduced mushrooming and reduced shortening. As the hardening is reduced, the extent of mushrooming increases. When hardening is completely suppressed the mushrooming becomes extreme as shown in Fig. 26(D), demonstrating the role of strain hardening in locally constraining deformation and making plastic deformation progress axially up the cylinder.

Also the extent of rebound is reduced with reduced hardening, as confirmed by time-resolved KE profiles. Fig. 27 shows residual profiles for the five different cases for impact of a 25.4 mm rod at 265 m s^{-1}. The nature of the observations is similar to those for the 76.2 mm rod. These observations also indicate that accurate stress–strain behavior prediction is necessary for an accurate prediction of the rod profile.
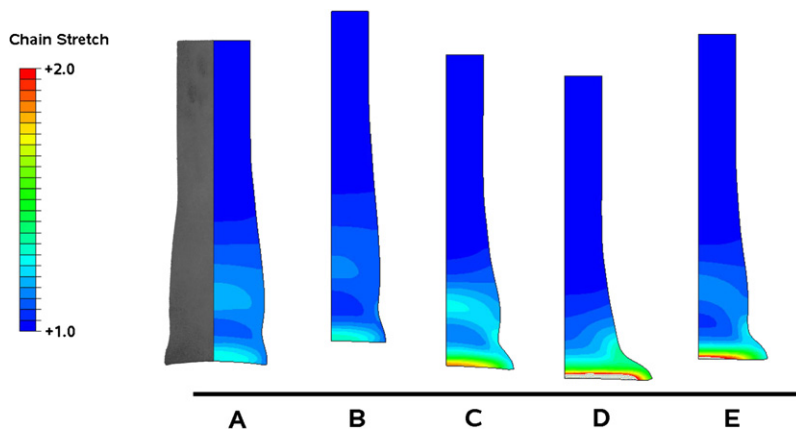

Fig. 26. Effect of variation in stress–strain behavior on the residual profile for a 76.2 mm rod impacting at 277 m s^{-1}.
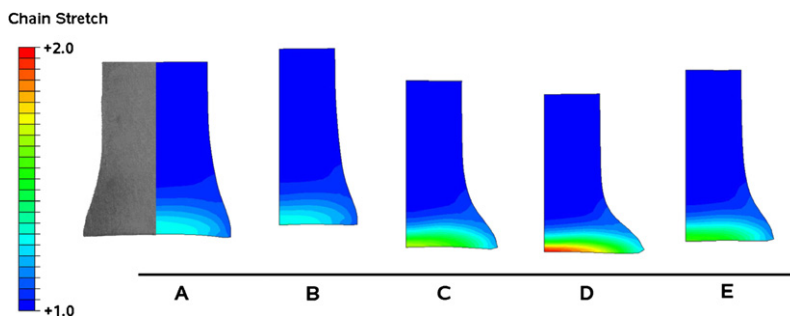

Fig. 27. Effect of variation in stress–strain behavior on the residual profile for a 25.4 mm rod impacting at 277 m s^{-1}.

6. Summary

Polymeric materials have been found to be effective materials for use in numerous applications requiring mechanical performance under high-rate loading conditions, ranging from golf balls to safety glass windows to transparent canopies and armor. The ability to accurately model and predict the mechanical behavior of a polymer during high-rate inhomogeneous deformations will enable optimized design of polymeric materials and structures to withstand impact loading. This paper experimentally documented the progression of inhomogeneous deformation in initially cylindrical rods of polycarbonate during high-rate impacts into a rigid wall, i.e. Taylor impact testing. Although, Taylor testing is widely used to observe and characterize high-rate plastic deformation in metals, there are few reports in the literature on polymers. In the case of long rods, the rod deformations are characterized by the formation of a mushroom head at the impact end with a subsequent radial barreling and distinctive lip formation. The precise shape depended upon the initial velocity of the rod. The shorter rods exhibited a residual geometry with a mushroom head but no radial barreling. All specimens showed significant shortening. Furthermore, the ability to accurately model and predict the observed progressions of deformation in the specimens during the impact events was demonstrated where a recently developed elastic–viscoplastic constitutive model for the high-rate deformation of polymers was utilized together with finite element analysis to accomplish the simulations. The simulations were true predictions in the sense that no information from the Taylor impact experimental results was utilized to fit the model. The simulations were found to be truly predictive of the high-rate events capturing all features of the progression in inhomogeneous deformations during these dynamic loading scenarios as shown through a direct comparison between high-speed photographic images and simulations at numerous stages of the event duration. The simulations also revealed the nature of interaction of plastic fronts and corresponding shear banding with the stress waves in the specimen, leading to the end geometry profiles. The ability to simulate these events enabled a parametric study of the effect of key features of the polymer stress–strain behavior on the progression of deformation during impact duration, revealing the role of softening in providing increased radial flow at the impact end and, perhaps more importantly, the role of strain hardening in stabilizing local deformation and hence propagating the inelastic deformation event axially up the cylinder involving a greater percent of the cylinder in absorbing the energy of impact. These results demonstrate the effectiveness of the constitutive model to predict complex, inhomogeneous, high-rate deformations in polymeric solids and hence are a step towards using such simulations to design polymers and structures for high-rate loading applications.

Acknowledgements

References

Arruda, E., Boyce, M.C., 1993. Evolution of plastic anisotropy in amorphous polymers during finite straining. International Journal of Plasticity 9, 697–720.

Arruda, E.M., Boyce, M.C., Jayachandran, R., 1995. Effects of strain rate, temperature and thermomechanical coupling on the finite strain deformation of glassy polymers. Mechanics of Materials 19 (2–3), 193–212.

Bauwens, J., 1972. Relation between the compression yield stress and mechanical loss peak of bisphenol-A-polycarbonate in the β transition range. Journal of Materials Science 7, 577–584.

Boyce, M.C., Parks, D., Argon, A., 1988. Large inelastic deformation of glassy polymers. Part I: Rate dependent constitutive model. Mechanics of Materials 7, 15–33.

Boyce, M.C., Arruda, E., Jayachandran, R., 1994. The large strain compression, tension and simple shear of polycarbonate. Polymer Engineering and Science 34, 716–725.

Briscoe, B.J., Hutchings, I.M., 1976. Impact yielding of high density polyethylene. Polymer 17, 1099–1102.

Carrington, W.E., Gayler, M.L.V., 1948. The use of flat-ended projectiles for determining dynamic yield stress III – Changes in microstructure caused by deformation under impact at high striking velocities. Proceedings of the Royal Society of London. Series A, Mathematical and Physical Sciences 194, 323–331.

Gillis, P.P., Jones, S.E., Dehn, M.H., 1987. Some further results on the Taylor impact test. Mechanics of Materials 6 (3), 293–301.

Hawkyard, J.B., 1969. A theory for the mushrooming of flat-ended projectiles impinging on a flat rigid anvil using energy considerations. International Journal of Mechanical Sciences 11, 313–324.

Hawkyard, J.B., Eaton, D., Johnson, W., 1968. The mean dynamic yield strength of copper and low carbon steel at elevated temperatures from measurements of the 'mushrooming' of flat-ended projectiles. International Journal of Mechanical Sciences 10, 929–930.

Holt, W.H., Mock Jr., W., Zerilli, F.J., Clark, J.B., 1994. Experimental and computational study of impact deformation of titanium Taylor cylinder specimens. Mechanics of Materials 17, 195–201.

House, J.W., Lewis, J.C., Gillis, P.P., Wilson, L.L., 1995. Estimation of flow stress under high rate plastic deformation. International Journal of Impact Engineering 16 (2), 189–200.

Hutchings, I.M., 1979. Estimation of yield stress in polymers at high strain-rates using G.I. Taylor's impact technique. Journal of the Mechanics and Physics of Solids 26, 289–301.

Jia, D., Ramesh, K.T., 2004. A rigorous assessment of benefits of miniaturization in the Kolsky bar system. Experimental Mechanics 44 (5), 445–454.

Johnson, M.D., 2001. Deformation and fracture of polycarbonate and rubber-modified polycarbonate under controlled temperature, deformation rate and notch stress triaxiality. Master's Thesis, Massachusetts Institute of Technology.

Jones, S.E., Gillis, P.P., Foster Jr., J.C., 1987. On the equation of motion of the undeformed section of a Taylor specimen. Journal of Applied Physics 61 (2), 499–502.

Jones, S.E., Maudlin, P.J., Gillis, P.P., Foster Jr., J.C., 1992. An analytical interpretation of high strain rate material behavior during early time plastic deformation in the Taylor impact test. In: Computers in Engineering, Proceedings Computers in Engineering Conference and Exposition – 1992, San Francisco, Transactions of ASME, vol. 2, pp. 173–179.

Jones, S.E., Maudlin, P.J., Foster Jr., J.C., 1997. An engineering analysis of plastic wave propagation in the Taylor test. International Journal of Impact Engineering 19 (2), 95–106.

Jones, S.E., Drinkard, J.A., Rule, W.K., Wilson, L.L., 1998. An elementary theory for the Taylor impact test. International Journal of Impact Engineering 21 (1), 1–13.

Kolsky, H., 1949. An investigation of the mechanical properties of materials at very high rates of loading. Proceedings of the Physical Society. Series B, Mathematical and Physical Sciences 62 (B), 676–701.

Maudlin, P.J., Bingert, J.F., House, J.W., Chen, S.R., 1999. On the modeling of the Taylor cylinder impact test for orthotropic textured materials: experiments and simulations. International Journal of Plasticity 15, 139–166.

Maudlin, P.J., Bingert, J.F., Gray III, G.T., 2003. Low-symmetry plastic deformation in BCC Tantalum: experimental observations, modeling and simulations. International Journal of Plasticity 19, 483–515.

Millet, J.C.F., Bourne, N.K., Stevens, G.S., 2006. Taylor impact of polyether ether ketone. International Journal of Impact Engineering 32 (7), 1086–1094.

Mulliken, A.D., 2006. Mechanics of amorphous polymers and polymer nanocomposites during high-rate deformation. Doctoral Thesis, Massachusetts Institute of Technology.

Mulliken, A.D., Boyce, M.C., 2004. Low to high strain rate deformation of amorphous polymers. In: Proceedings of the 2004 SEM X International Congress and Exposition on Experimental and Applied Mechanics, Costa Mesa, CA, Paper No. 197.

Mulliken, A.D., Boyce, M.C., 2006. Mechanics of rate-dependent elastic–plastic deformation of glassy polymers from low to high strain rates. International Journal of Solids and Structures 43 (5), 1331–1356.

Nimmer, R.P., Woods, J.T., 1992. An investigation of brittle failure in ductile notch-sensitive thermo-plastics. Polymer Engineering and Science 32, 1126–1137.

Rae, P.J., Gray, G.T., Dattelbaum, D.M., Bourne, N.K., 2004. The Taylor impact response of PTFE (Teflon). In: Proceedings: Shock Compression of Condensed Matter – 2003. American Institute of Physics, pp. 671–674.

Ree, T., Eyring, H., 1955. Theory for non-Newtonian flow I. Solid plastic system. Journal of Applied Physics 26, 793.

Socrate, S., Boyce, M.C., 2000. Micromechanics of toughened polycarbonate. Journal of the Mechanics and Physics of Solids 48 (2), 233–273.

Taylor, G., 1948. The use of flat-ended projectiles for determining dynamic yield stress I – Theoretical considerations. Proceedings of the Royal Society of London. Series A, Mathematical and Physical Sciences 194, 289–299.

Turgutlu, A., Al-Hassani, S.T.S., Akyurt, M., 1996. Impact deformation of polymeric projectiles. International Journal of Impact Engineering 18, 119–127.

Whiffin, A.C., 1948. The use of flat-ended projectiles for determining dynamic yield stress II – Tests on various metallic materials. Proceedings of the Royal Society of London. Series A, Mathematical and Physical Sciences 194, 300–322.

Wilkins, M.L., Guinan, M.W., 1973. Impact of cylinders on a rigid boundary. Journal of Applied Physics 44 (3), 1200–1206.